

This article was downloaded by:[2007 Korea University - Seoul Campus]  
[2007 Korea University - Seoul Campus]

On: 11 June 2007

Access Details: [subscription number 768980396]

Publisher: Taylor & Francis

Informa Ltd Registered in England and Wales Registered Number: 1072954

Registered office: Mortimer House, 37-41 Mortimer Street, London W1T 3JH, UK



## Drying Technology An International Journal

Publication details, including instructions for authors and subscription information:  
<http://www.informaworld.com/smpp/title-content=t713597247>

### A Modeling Investigation of Suppressant Distribution from a Prototype Solid-Propellant Gas-Generator Suppression System into a Simulated Aircraft Cargo Bay

To cite this Article: Yoon, S. S., Kim, H. Y., Hewson, J. C., Suo-Anttila, J. M., Glaze, D. J. and DesJardin, P. E. , 'A Modeling Investigation of Suppressant Distribution from a Prototype Solid-Propellant Gas-Generator Suppression System into a Simulated Aircraft Cargo Bay', Drying Technology, 25:6, 1011 - 1023  
To link to this article: DOI: 10.1080/07373930701396410

URL: <http://dx.doi.org/10.1080/07373930701396410>

PLEASE SCROLL DOWN FOR ARTICLE

Full terms and conditions of use: <http://www.informaworld.com/terms-and-conditions-of-access.pdf>

This article maybe used for research, teaching and private study purposes. Any substantial or systematic reproduction, re-distribution, re-selling, loan or sub-licensing, systematic supply or distribution in any form to anyone is expressly forbidden.

The publisher does not give any warranty express or implied or make any representation that the contents will be complete or accurate or up to date. The accuracy of any instructions, formulae and drug doses should be independently verified with primary sources. The publisher shall not be liable for any loss, actions, claims, proceedings, demand or costs or damages whatsoever or howsoever caused arising directly or indirectly in connection with or arising out of the use of this material.

© Taylor and Francis 2007

# A Modeling Investigation of Suppressant Distribution from a Prototype Solid-Propellant Gas-Generator Suppression System into a Simulated Aircraft Cargo Bay

S. S. Yoon,<sup>1</sup> H. Y. Kim,<sup>1</sup> J. C. Hewson,<sup>2</sup> J. M. Suo-Anttila,<sup>2</sup> D. J. Glaze,<sup>3</sup>  
and P. E. DesJardin<sup>4</sup>

<sup>1</sup>Mechanical Engineering Department, Korea University, Sungbukgu, Seoul, Korea

<sup>2</sup>Fire Science & Technology, Sandia National Laboratories, Albuquerque, New Mexico, USA

<sup>3</sup>School of Mech Engineering, Purdue University, West Lafayette, Indiana, USA

<sup>4</sup>Department of Mechanical & Aerospace Engineering, University of Buffalo, Buffalo, New York, USA

---

One new technology for fire suppressant distribution in total-flooding applications is the solid-propellant gas-generator (SPGG) technology. This article presents experimental and modeling studies of one such prototype system in order to better understand observations in the testing of this system. This particular SPGG system generates fine particles that act to suppress any fire in conjunction with inert gases also generated in the SPGG system. Initial conditions for the simulations are obtained from the available measurements of the prototype system. The modeling provides key information related to the distribution of the particles and their potential effectiveness as a fire suppressant. The primary variable in the SPGG design as identified in the initial measurements, also presented here, was the particle size, with typical particle sizes being measured at 2 and 15  $\mu\text{m}$ . The key modeling result is that there is a tradeoff between the most uniform distribution of particles and the available surface-to-volume ratio for chemical suppression. Information is also provided regarding the thermal dissipation from the SPGG system.

---

**Keywords** Distribution; Fire suppression; KBr; Stochastic separated flow mode; Suppressant

## INTRODUCTION

The cessation of production for Halon-based fire suppressants has led to substantial research in alternative fire suppression technologies for total-flooding applications.<sup>[1]</sup> In total-flooding applications the objective is to extinguish a fire without the need for a human to enter a compartment. Such systems are often employed in unoccupied aircraft compartments like the simulated aircraft cargo bay considered here. Many of the alternative systems have

had less desirable characteristics than the Halon-based suppression. In particular, the suppression system mass for hydrofluorocarbon suppression systems is often about twice that of the equivalent Halon-based system.<sup>[2]</sup> Because the system mass is a key concern in aerospace applications, other technologies have been explored. One alternative suppression technology with potentially reduced system mass is the solid-propellant gas generators (SPGG). SPGG systems work by generating, through the rapid combustion of a solid propellant, product gases that can dilute reactants and lead to suppression. The primary products from a typical solid propellant are  $\text{N}_2$ ,  $\text{CO}_2$ , and  $\text{H}_2\text{O}$ . For the particular SPGG system of interest here,<sup>[3]</sup> additional components of the propellant mixture condense to form a fine particulate. These particulates are thought to add significantly to suppression capabilities through surface chemistry. The particulate products found in the SPGG system tested are  $\text{K}_2\text{CO}_3$  and KBr, the latter containing bromine (Br). Bromine is thought to be the element providing much of the chemical suppression effect in Halon and also the element contributing most significantly to the ozone depletion problems in Halons.<sup>[4]</sup> The inclusion of Br in the precipitated salt form in Goodrich-244 is believed to provide an environmentally favorable form with which the chemical benefits of Br can be utilized. Olander<sup>[3]</sup> provides further detail on the theory of SPGG fire suppression, specifically applied to the Goodrich-244 system under consideration herein. Also available in Olander<sup>[3]</sup> are results from tests conducted with the Goodrich-244 system that indicate substantially less suppressant is required, compared to Halon-1301, on a per mass and per volume basis for suppression in simulated aircraft cargo bays.

---

Correspondence: S. S. Yoon, Mechanical Engineering Department, Korea University, Anamdong, 5-Ga, Sungbukgu, Seoul, 136-713, Korea; E-mail: skyoon@korea.ac.kr

The Goodrich-244 system is currently under consideration for application to cargo bay fire suppression. The purpose of this article is to provide computational modeling results that address several questions that arise in the application of SPGG systems as highlighted by the tests of this prototype system. To this end, this article first discusses the overall observations and particle measurements conducted during the test. These measurements act as boundary conditions for the computational modeling. Following this, the modeling approach is presented; in brief, the gas-phase flow is modeled in the traditional manner while the particle field is computed using a Lagrangian approach that is fully coupled with the gas-phase solution. This is followed by the results and discussion in the context of the application of SPGG systems to aircraft cargo bays and similar systems. Several concerns that arise in the application of SPGG systems are addressed in that section. One concern is how uniformly the particulates are distributed within the cargo bay and how rapidly they settle out or stick to surfaces. Particle number density predictions are provided as a function of time in the simulated cargo bay application. Because the surface reactivity is postulated to play a role in the fire suppression effectiveness, the particle surface area is contrasted with the number density. The relatively high temperature of the SPGG effluent and the associated heat flux to the near-injector region is also of concern; therefore, heat flux estimates to the ceiling are provided.

## PARTICLE MEASUREMENTS

One of the products of the solid-propellant combustion is a particulate composed primarily of KBr. A series of particle size and composition measurements were conducted to characterize this particulate. As indicated in the Discussion section, the particle size plays an important role in both the uniformity of the distribution of the particles and in the effectiveness of fire suppression. Two methods were employed to measure particle characteristics: thermophoretic sampling onto a grid for use in transmission electron microscopy and bulk sampling for use with scanning electron microscopy. The former technique allows detailed analysis of particles in the 1  $\mu\text{m}$  and smaller size class while the latter is best suited for larger particles.

## TEM Particulate Images

The particulate produced by the SPGG system was thermophoretically sampled to assess the morphology, including the size distribution and shape of the particulates. The thermophoretic sampling device was designed to collect particulates for transmission electron microscopy (TEM) analysis by briefly exposing an electron microscope grid such that particulates are deposited on the grid surface via combined impingement and thermophoresis. The use of this

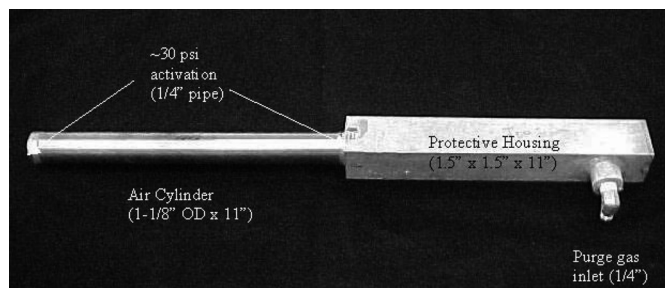


FIG. 1. Overall photograph of particulate sampler.

diagnostic was successfully demonstrated in harsh environments, including large pool fires and propellant fires.<sup>[5]</sup>

The device consisted of a solenoid-actuated piston-cylinder assembly with pressurized nitrogen gas activation to quickly expose the electron microscope grid to the combustion products. The two titanium TEM grids (0.11 cm diameter) were mounted to a 0.32-cm-thick grid holder using a 0.08-cm-thick aluminum plate. The grid holder was fastened to a non-rotating rod of the air cylinder and was enclosed in a 25-cm-long, low-flow, nitrogen-purged protective housing. Two baffles were positioned at the exit of the protective housing to reduce the probability of stray particle deposition on the grids prior to exposure. Photographs of the particulate sampling diagnostic are shown in Figs. 1 and 2.

During sampling, the air cylinder was pressurized such that the grids were extended 8 cm from the end of the protective housing for a few minutes. Following the experiment, the grids were removed from the holder and directly inserted in the TEM for analysis. The particle morphology was determined directly from the TEM images using an application that allows the user to automatically select the particle and determine the diameter, length, width, radius of gyration, etc.

Thermophoretic sampling was performed at various distances from the exit of the generator. The three sampling points were at locations 5.1, 30.5, and 61 cm from the exit of the generator, the locations at which the thermocouples

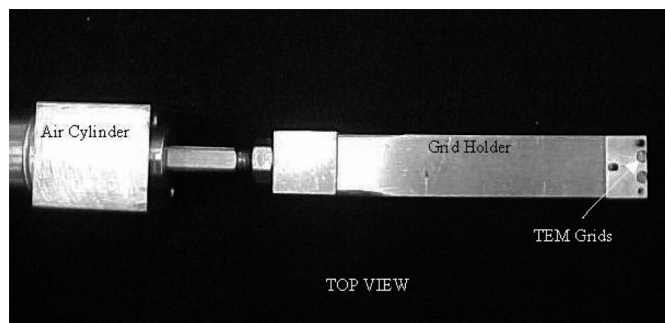


FIG. 2. Grid holder photographs.

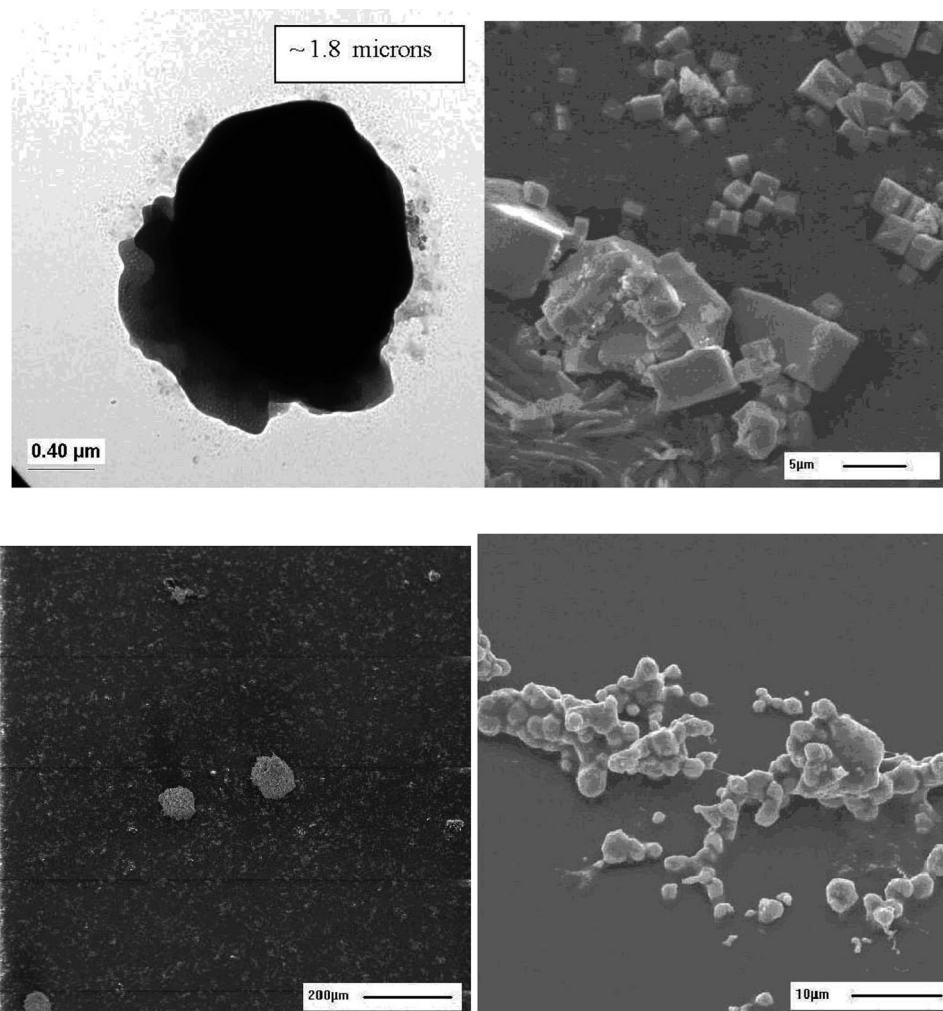


FIG. 3. Particulate collected at TEM grids.

measuring local gas temperature were also placed. During the experiment it took approximately 25 s for the propellant to fully ignite. The particulate sample was obtained approximately 2 s after it was fully ignited.

The TEM grids were imaged and analyzed for particulate information. The particle images shown in Fig. 3 indicate that substantial mass in the TEM-measurable size range is in particles between 0.5 and 2  $\mu\text{m}$ . There is evidence that larger particles are aggregated with (or possibly from) smaller particles. In general, the particles are spherical at this scale. There are also smaller particles in the 10-nm size range evident in the images. The large spheres were measured using an internally developed sizing program. The spheres were found to be 0.78 and 1.8  $\mu\text{m}$ .

#### SEM Particulate Images

SEM (scanning electron microscopy) images were obtained with samples collected into a Petri dish and also

a vacuum flask. For both samples, material was collected from the surface of the containment vessel using double-stick carbon films. The film was gently pressed against the surface and then transferred to a holder block. Material from the surface of the vessel was trapped by the sticky carbon and thereby made available for SEM and EDS (energy-dispersive spectrometer) analysis.

The analysis concluded that particulate was primarily composed of K and Br in the shape of either cubes or spheres. Unfortunately, the collection methods did not permit many individual particles or agglomerates to be imaged; therefore, it was very difficult to quantify the true morphology as emitted from the generator. In addition, the transfer of the sample from the containment vessel to the holder block could potentially alter the morphology. The images obtained during these experiments, shown in Fig. 3, were analyzed to determine whether an estimate of the particulate morphology could be obtained to facilitate the model calculations.

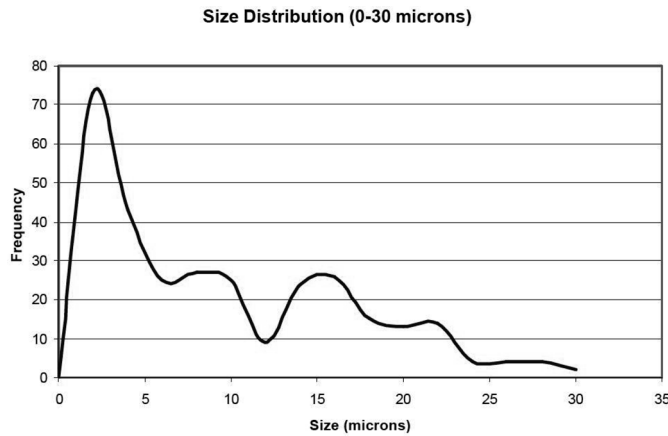


FIG. 4. Goodrich particulate distribution up to 30  $\mu\text{m}$ .

The images in Fig. 3 are quite diverse, making it difficult to identify dominant features. Nevertheless, an attempt was made to determine the size of a large number of particles on each of the images. A very broad distribution of sizes was observed (0.02–100  $\mu\text{m}$ ) although the majority of the particles and aggregates were less than 40  $\mu\text{m}$ . The detailed distribution for the images of Fig. 3 is shown in Fig. 4. The detailed distribution concentrates on the particles less than 30  $\mu\text{m}$  (about 10 particles were eliminated that were above this threshold). This detailed view allows for a determination of the dominant particle sizes. Based upon the analysis, particle sizes of 2 and 15  $\mu\text{m}$  have been selected for use in simulations as discussed in the following section.

## SIMULATIONS

Simulations have been conducted using Sandia's Vulcan fire-physics code. Vulcan solves the Reynolds-averaged Navier-Stokes equations, coupled with equations for species, enthalpy (from which temperature is obtained), and the turbulent kinetic energy and dissipation (the  $k\text{-}\epsilon$  model)<sup>[6]</sup> using standard modeling approaches<sup>[7]</sup> and numerical methods.<sup>[8]</sup> In addition to the gas-phase species, condensed-phase particles are transported using a Lagrangian method coupled to the Eulerian grid. This particle transport model employs an ensemble of parcels of particles to represent the evolution of the particle location, velocity, size, and temperature distribution.<sup>[9–13]</sup> There is a stochastic component to the parcel evolution that acts to model particle dispersion due to unresolved turbulence.<sup>[10,11]</sup> Additional dispersion of particles within a single parcel is modeled as in Zhou and Yao.<sup>[12]</sup> The overall particle gas-phase approach is similar to the approach used in the popular internal combustion engine simulation code, KIVA.<sup>[14,15]</sup> The model uses parcels to represent a large number of individual particles, typically a billion individual particles; these parcels are transported according to calculated force balances on individual particles. A large number

of such parcels (tens or hundreds of thousands) are tracked to describe the spatial evolution of the condensed phase and its size distribution. The fact that the parcels have finite extent allows a significantly smaller number of parcels to adequately represent the particle field distribution.<sup>[12]</sup> Properties of particles, including their size, temperature, composition, and thermal properties like specific heat, density, drag coefficients, etc., are associated with parcels. Particles are subject to transport by the mean flow and by turbulent fluctuations.

When a particle collides with a solid wall, it is assumed to stick to the wall if the impact velocity (kinetic energy) is sufficiently high and bounces otherwise. In general, sticking is the predominant result of collisions for the particles considered here. Because the adhesion of the particles is unknown, this is neglected in the current study. As such, we expect the present simulations to underestimate the particle spreading following wall impingement.

## Stochastic Separated Flow Conservation Equations

When using the Lagrangian particle transport model the particle velocities evolve according to a force balance.<sup>[16]</sup> Aerodynamic drag and the gravitational body force have been identified as the dominant external forces acting on suspended particles. As such, the equation of particle motion can be expressed as:

$$\frac{d\vec{u}_p}{dt} = \frac{C_D}{8} \rho_g \pi D_p^2 |\vec{u}_g - \vec{u}_p| (\vec{u}_g - \vec{u}_p) + \frac{\pi}{6} D_p^2 (\rho_p - \rho_g) \vec{g} \quad (1)$$

where  $\vec{u}_p$  and  $\vec{u}_g$  are the particle and gas velocities,  $\rho_p$  and  $\rho_g$  are the particle and gas density,  $C_D$  is the aerodynamic drag coefficient,  $D_p$  is the particle diameter, and  $\vec{g}$  is the gravity vector. A correlation is used for  $C_D$  that allows for the observed cubic shape of the KBr particles.<sup>[17,18]</sup> The particle momentum change due to drag is offset by a change in the gas momentum to conserve overall system momentum. An energy balance for particles can similarly be written

$$m_p c_{vp} \frac{dT_p}{dt} = \pi D_p \frac{\mu_g c_{pg}}{\text{Pr}_g} (T_g - T_p) Nu_g \quad (2)$$

where  $c_{vp}$  is the constant-volume specific heat of particle,  $c_{pg}$  is the constant-pressure specific heat of gas,  $\mu_g$  is the dynamic viscosity of gas,  $\text{Pr}_g = \nu_g / \alpha_g = c_{pg} \mu_g / k_g$  is the gas Prandtl number,  $Nu_g$  is the gas Nusselt number, and  $T_g$  and  $T_p$  are the surrounding gas and particle temperatures, respectively. Energy changes associated with cooling of particles are offset in the gas phase by heating of the surrounding gases. These ordinary differential Eqs. (1) and (2) are solved for every parcel using the LSODES library.<sup>[19]</sup>

The changes in the particle field momentum and energy according to Eqs. (1) and (2) must be reflected in the gas-phase momentum and energy conservation. This is done

using a conservative approach based on differencing the initial and final particle states over a time step,  $\Delta t$ . The momentum and energy source terms are then:

$$\begin{aligned} S_{mom,i} &= -\frac{1}{V_{cell}} \sum_{N_p} \frac{\Delta(m_p u_{p,i})}{\Delta t} \\ S_{energy} &= -\frac{1}{V_{cell}} \sum_{N_p} \frac{\Delta(m_p h_{p,i})}{\Delta t} \end{aligned} \quad (3)$$

where  $h_{p,i}$  is the enthalpy of the particle. Further details regarding the implementation of the Lagrangian model are provided in DesJardin and Gritzol.<sup>[20]</sup>

### Equilibrium Particle Methodology

From Eqs. (1) and (2) above, one can estimate the relaxation times for particle velocity and temperature, that is, time over which particle velocities and temperatures change significantly, to be

$$\tau_v = \frac{\rho_p D_p^2}{18\mu_g} \left( \frac{24}{C_D Re_p} \right) \quad (4)$$

for the velocity and

$$\tau_T = \frac{m_p}{\pi D_p \mu_g} \left( \frac{c_{vp}}{c_{vg}} \right) \left( \frac{Pr_g}{Nu_g} \right) \quad (5)$$

for the temperature. In Eqs. (4) and (5),  $Re_p = U_{rel} D_p / \nu_g$  is the Reynolds number based on the relative velocity between the particle and the gas;  $c_{vp}$  and  $c_{vg}$  are the constant-volume specific heat of the particle and the gas, respectively; and  $Pr_g$  and  $Nu_g$  are the gas Prandtl and Nusselt numbers, respectively. For the current scenario, the relaxation times defined in Eqs. (4) and (5) are much smaller than the characteristic times for the gaseous flow. To solve Eqs. (1) and (2) with small relaxation times would require either a very small time step, increasing computational cost by roughly an order of magnitude, or an unacceptable reduction in the model accuracy and stability. These small relaxation times indicate that the particle will closely follow the flow, as opposed to larger values indicating a more ballistic trajectory independent of the carrier gas.

For those cases where particles will closely follow the flow, an alternative solution strategy is adopted, referred to as the “equilibrium particle method” because the gas and particle velocities and temperatures are assumed to be equilibrated. In this method, the particle momentum and the gas-phase momentum are equilibrated within a grid cell at the beginning of the time step according to the relation

$$m_g u_g + \sum_{i=1}^{N_{eq}} (m_p u_p)_i = m_g u_{eq} + \sum_{i=1}^{N_{eq}} (m_p u_{eq})_i \quad (6)$$

where the left and right sides of the equation represent the

state before and after equilibration, velocities being equal after equilibration. It is this equilibrium velocity,  $u_{eq} = u_{eq,g} = u_{eq,p}$ , that is obtained from the solution of Eq. (6). In Eq. (6), the summation over  $N_{eq}$  is the summation over the number of equilibrium particles in the grid cell and  $m_g$  is the mass of the gas in the cell. Similarly, the temperatures are equilibrated using an energy balance

$$\begin{aligned} m_g \left( h_g - RT_g + \frac{u_g^2}{2} \right) + \sum_{i=1}^{N_{eq}} m_{p,i} \left( c_{vp} T_p + \frac{u_p^2}{2} \right)_i \\ = m_g \left( h_g - RT_{eq} + \frac{u_{eq}^2}{2} \right) + \sum_{i=1}^{N_{eq}} m_{p,i} \left( c_{vp} T_{eq} + \frac{u_{eq}^2}{2} \right)_i \end{aligned} \quad (7)$$

to obtain  $T_{eq}$ . Because the gas velocity and temperature are altered in this equilibration process, there is two-way coupling between the gas phase and particle field. The changes in the particle field momentum and energy are thus reflected in an effective source term in the gas-phase evolution equations that ensures overall conservation of momentum and energy. All particles with either  $\tau_v$  or  $\tau_T$  smaller than 1% of the gas time step are classified as equilibrium particles, while all others are non-equilibrium particles. Note that equilibration during one time step does not imply that equilibrium exists at the beginning of the subsequent time step because the gas-phase properties and the particle velocities change due to turbulent mixing in a non-identical manner.

### Computational Details

The particular configuration investigated consists of a dual-slot SPGG system mounted on the ceiling of a DC-10 cargo bay mockup as shown in Fig. 5. This configuration is similar to the compartment geometry in which aircraft cargo bay suppression systems are certified except for the fact that the simulation neglects the taper found in the lower sections. The overall physical dimensions are  $10 \times 3.7 \times 1.65$  m and a grid resolution of  $120 \times 30 \times 30$  is

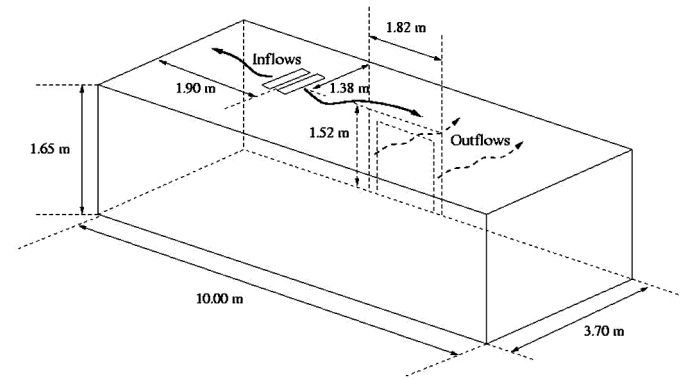


FIG. 5. Simulated DC-10 cargo bay.

employed in the computational model. The SPGG system is mounted toward one end and off of the centerline to match the system location. Outflow to maintain a constant chamber pressure is through an array of openings centered on one wall as shown in Fig. 5 to simulate leakage around a cargo door. Inlet air flow from airframe leakage was neglected, the only inlet coming from the SPGG system.

The fire suppressant leaves the propellant injector through a pair of slots that are positioned so that the effluent tends to flow out (away from the adjacent slot) more than down. To obtain some estimates of the angle at which the flow should leave the slots, a series of numerical simulations of the propellant injector were conducted. In these simulations, particles were neglected, considering only the gas phase. This approach was motivated by the nature of the particle formation: the particles are assumed to condense out of the gas-phase products at some point

downstream of the actual propellant combustion. This propellant combustion is not directly modeled but rather is represented by a mass source term on the top and two side surfaces nearest the slots. The total mass flux from these surfaces is based on estimates obtained from Goodrich as to the mass burning rate being in the vicinity of 2 lb m/s or 0.91 kg/s. This mass-burning rate was used in all of the present simulations. The time series snapshots of the injected KBr particles are seen in Fig. 6. The thermocouple placed at location 1 is hidden inside the KBr cloud in the upper ceiling of the containment vessel. At  $t = 10$  s, the container is filled with KBr, leaving high particle concentration in the upper half of the container.

Figure 7 shows the flow pattern in and near the injector as predicted using Vulcan. Because the products of propellant combustion are hot, assumed here to be 1200 K based on thermodynamic estimates, buoyancy and the Coanda

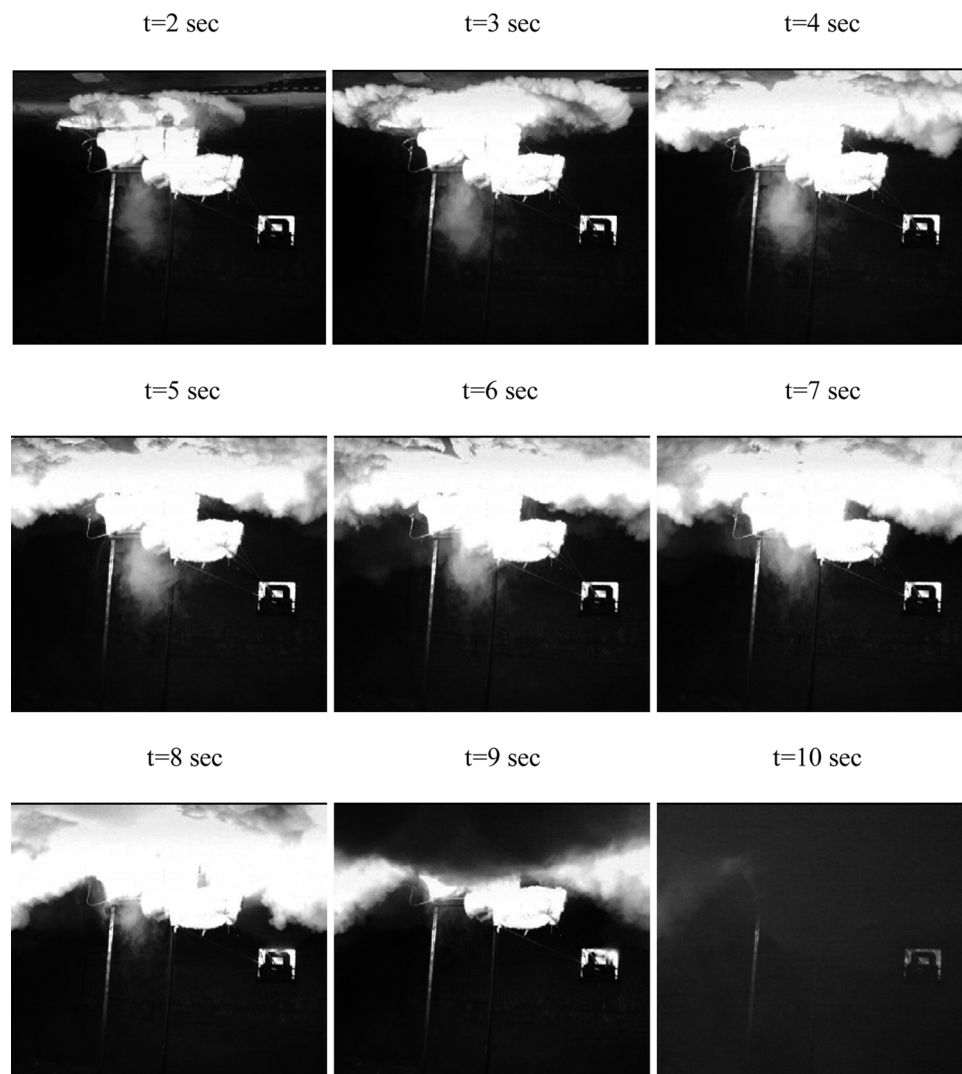


FIG. 6. Snapshots of the KBr particles injected from containment vessel. The particles were injected as of  $t = 0$  sec.

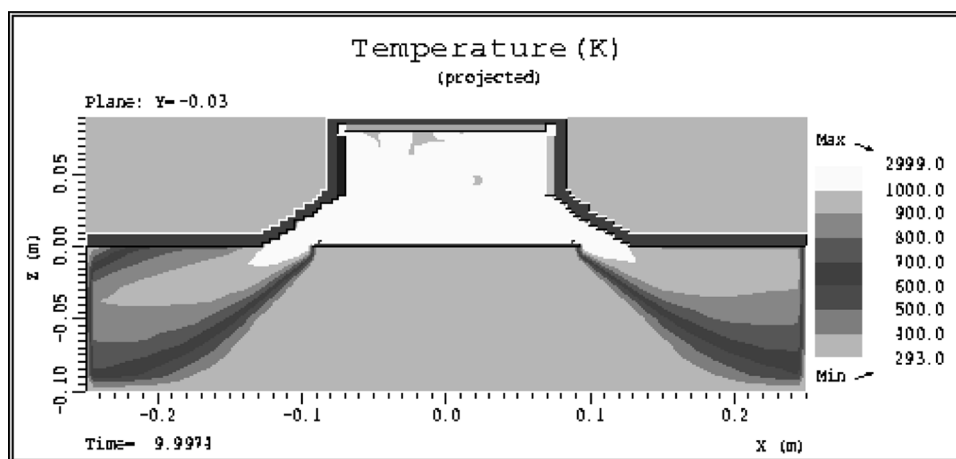


FIG. 7. Simulation of SPGG injector cross section showing temperature contours near injection slots.

effect cause the suppressant to flow along the ceiling. Prior to being moved toward the ceiling, the flow exits at an angle of roughly  $35^\circ$  below the horizontal plane. In the full-scale simulations of the cargo bay, the injector is not modeled in the detail shown in Fig. 7. Rather, the injector is modeled as a pair of slots. Based on these results, the initial flow direction for both the gas and particle flow at the injector exit slots are set to  $35^\circ$  below horizontal.

The suppressant composition at the injector exit was also determined from information provided by Olander.<sup>[3]</sup> The flow may be broken into gaseous ( $\text{CO}_2$ ,  $\text{H}_2\text{O}$ , and  $\text{N}_2$ ) and condensed solid components ( $\text{KBr}$  and  $\text{K}_2\text{CO}_3$ ). Given the mass burning rate of the propellant and the composition described in the previous paragraph, the gaseous flow rate through the pair of slots will be  $0.029 \text{ kg/s}$ . Given the temperature and assuming 1 bar pressure, the resulting mean outflow velocity is found to be  $14.8 \text{ m/s}$ ; here a slot cross section area of  $3.23 \times 10^{-3} \text{ m}^2$  is used. If the suppressant is hotter or cooler at the exit, the velocity will vary in a manner directly proportional to the temperature. For example, if the suppressant exited at  $300 \text{ K}$ , roughly ambient, the velocity would be four times less,  $3.7 \text{ m/s}$ .

The particles exit the injector at the same velocity as the gas and in the same average direction ( $-35^\circ$ ). The initial direction for each individual parcel may vary by  $\pm 10^\circ$  from  $-35^\circ$  to simulate the initial spread of particles across the gas flow due to initial turbulent dispersion estimates (consequences of the turbulent velocity fluctuations).<sup>[17,18]</sup> The net particle mass flux is  $0.062 \text{ kg/s}$ . Particle and gas mass flux from the suppressant generator are split evenly across the two slots giving  $0.031 \text{ kg/s}$  in particle flux and  $0.0145$  in gas mass flux from each slot. Injection ends after 10 s when two pounds of propellant are consumed, the result of which produces the total number of particles,

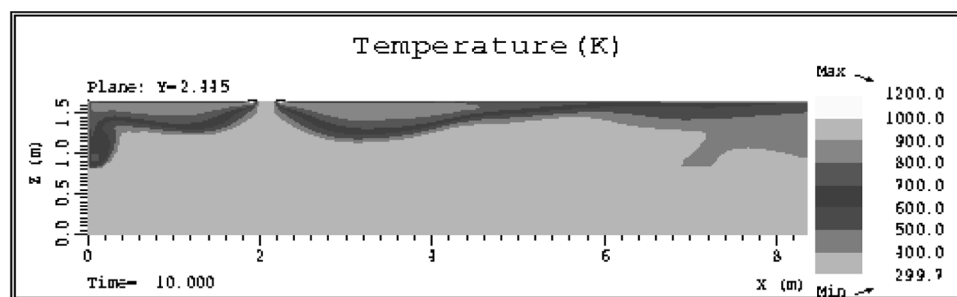
approximately  $1 \times 10^{14}$  and  $2 \times 10^{11}$  for 2 and  $15 \mu\text{m}$  cases, respectively.

Simulations were conducted with particles having average diameters of either 2 or  $15 \mu\text{m}$ , as discussed previously, with size distributions assumed to obey the Rosin-Rammler form. With a fixed mass flux, the number of particles injected is inversely proportional to the cube of the diameter so roughly 400 ( $7.5^3 = 422$ ) times as many smaller particles are injected than larger particles (the proportionality is not exact since the particle size distribution follows the Rosin-Rammler distribution). The total particle surface area is of interest in determining the surface catalytic effect; it is also greater, by a factor of the diameter ratio (7.5), for smaller particles. The particle densities and temperature are taken to be  $2300 \text{ kg/m}^3$  and  $1200 \text{ K}$ , and its size remains constant as  $\text{KBr}$  does not evaporate appreciably at these temperatures.

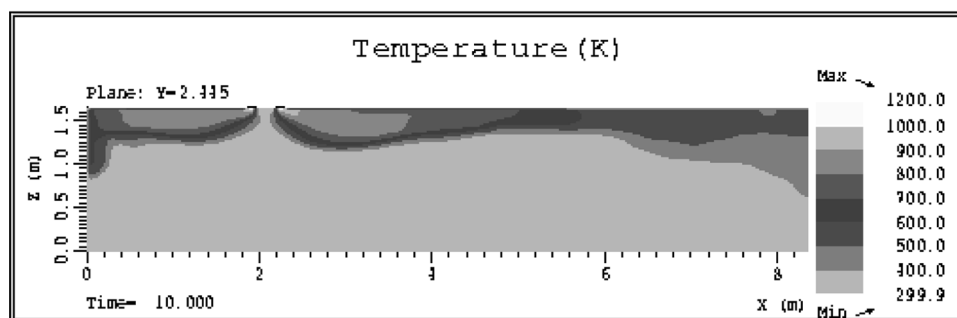
It is well known that the degree to which particles follow the flow, as opposed to having ballistic trajectories, is strongly dependent on their size. Small particles approach kinematic and thermodynamic equilibrium with the carrier gas more rapidly, as in Stokes flow. Results indicate that particles with  $D_p = 2 \mu\text{m}$  have velocity and temperature relaxation times on the order of  $10^{-5} \text{ s}$  while those with  $D_p = 15 \mu\text{m}$  have velocity and temperature relaxation times on the order of  $10^{-3} \text{ s}$ . With computational time steps on the order of  $10^{-3} \text{ s}$ , the smaller particles are generally treated with the equilibrium method through Eqs. (6) and (7) as described previously while the larger particles are evolved according to Eqs. (1) and (2) as described earlier.

## RESULTS AND DISCUSSIONS

In this section, results pertinent to the use of SPGG systems with a particle component,  $\text{KBr}$  particles here, will be presented and discussed. As indicated in the Introduction,



(a)



(b)

FIG. 8. Temperature contour plots along the cargo bay at the plane corresponding to the SPGG injector centerline at the end of injection (10 s). Mean particle diameters are (a) 15  $\mu\text{m}$  and (b) 2  $\mu\text{m}$ .

there are several questions that arise in the application of systems like these to total-flooding fire suppression. First, these systems are to be evaluated in terms of performance both in their ability to suppress fire and in their cost penalty relative to other competing systems. For the cost penalty we ignore monetary cost since information is not available and consider only the system mass that is important because, in aircraft applications, the suppression system mass directly displaces the cargo mass that can be carried. The ability to suppress fires will be measured by the degree of dispersion of the suppressant because the system is designed to suppress fires everywhere in the compartment. The degree of dispersion for particulate systems with potential surface reactivity<sup>[3]</sup> should be measured both in the overall distribution of the suppressant mass and the overall distribution of the particle surface area. At present, data are not available to properly weight these two measures in a combined suppression ability, so they will be considered separately. Other information available from the modeling results includes the role of the hot gases in undesirable heat flux.

Immediately after leaving the generator through the two slots, the hot suppressant gases and particles begin turbulent mixing with the ambient air. This cooling rapidly reduces the temperatures and suppressant concentrations

from their peak values but complete mixing takes substantial time. As such, hot gases and particles may move along the length of the cargo bay ceiling for both 2 and 15  $\mu\text{m}$  cases as shown in Fig. 8 before descending along the walls. The asymmetric location of the suppressant injector results in very different flow patterns in the two slots. The slot with flow directed toward the near wall will be referred to henceforth as the left slot and the slot with flow directed away from the near wall will be referred to as the right slot. The flow from the right slot is observed to move smoothly across the cargo bay ceiling. The flow from the left slot is rapidly hindered by the end wall, at which point the flow is forced down from the ceiling. Continued flow buoyancy causes the hot suppressants to roll back upwards in a vortical motion along the left wall as shown in Fig. 8; its vortical motion is more prominent in 15  $\mu\text{m}$  case in Fig. 8a. Figure 8 also shows that the particle size has a relatively small effect on the overall flow field, but the larger particles and gas flow cool more slowly and travel more closely to the ceiling because of greater buoyant acceleration. The validation of the modeling results is made between the computational results and the experimental data in Fig. 9, comparing the local gas temperature at locations 1 and 2. The thermocouples were situated at 0.40 (for location 1) and 0.15 m (for location 2) downward from the injector

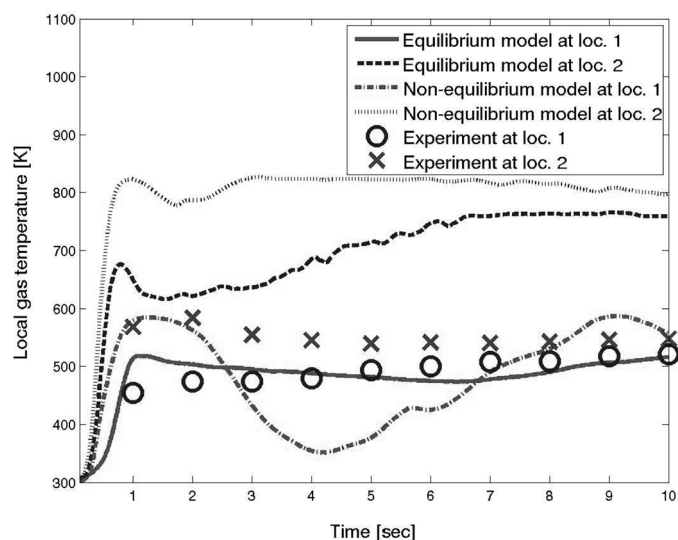


FIG. 9. Gas temperature comparison between computational results and experimental data.

slot. For both modeling and experimental results, the gas temperature at location 2 (closer to the injection slot) is higher. The equilibrium particle model seems to give better prediction at location 1, as compared to the results of the non-equilibrium model. This indicates that the KBr particles are better modeled with the Stokes flow. Near the injection slot of location 2, the deviation of the modeling prediction from the experimental data is shown in Fig. 9. The reason as to why predicted temperature is higher than the experimental data may be due to the over-prediction of the  $k-\epsilon$  turbulence mixing model, which may have yielded the overly higher gas local temperature.

Of significant concern for SPGG fire suppression systems is the heat flux from the hot suppressant mixture to surfaces. With ceiling-mounted SPGG systems, the most significant heat flux is to the ceiling near the injector outlet. Figure 10 shows the predicted convective heat flux, in the unit of  $W/m^2$  to the ceiling at the end of injection at 10 s for  $2\mu m$  case. Also shown in Fig. 10 is the near-ceiling

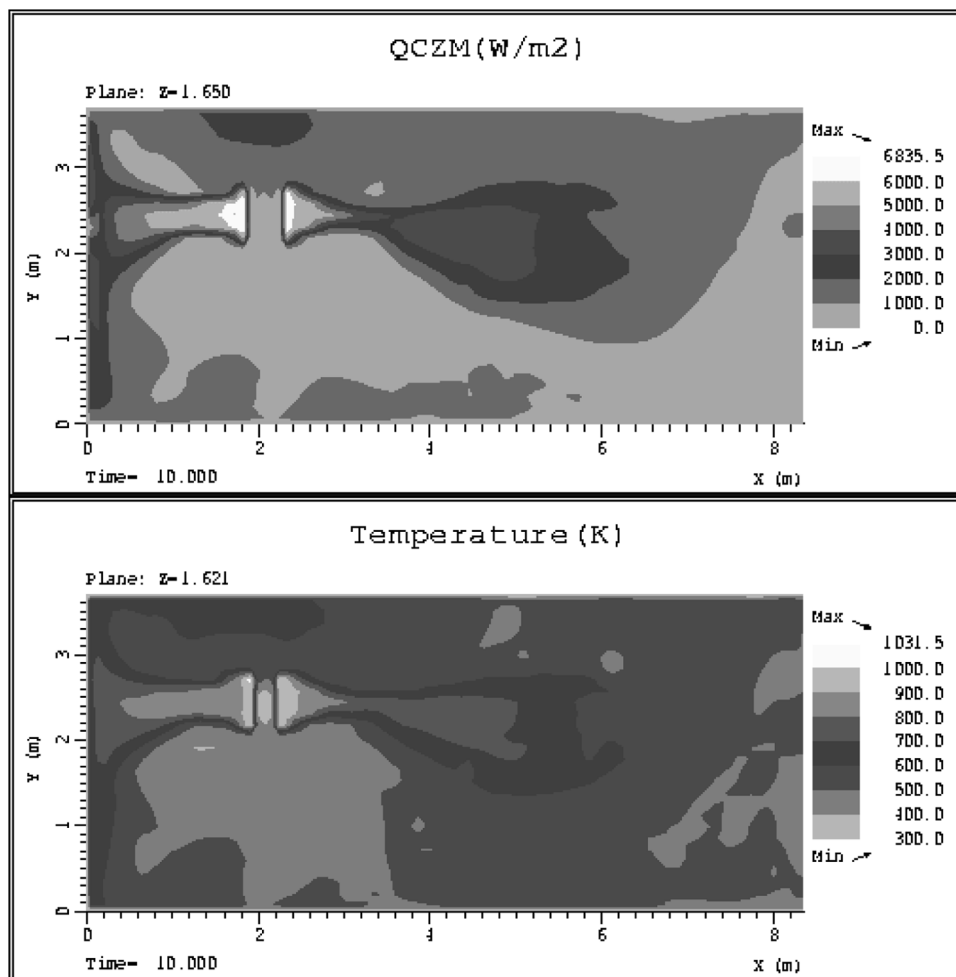


FIG. 10. Heat flux to the cargo bay ceiling (top) and the gas temperature near the ceiling (bottom) at the end of injection (10s). Mean particle diameters are  $2\mu m$ .

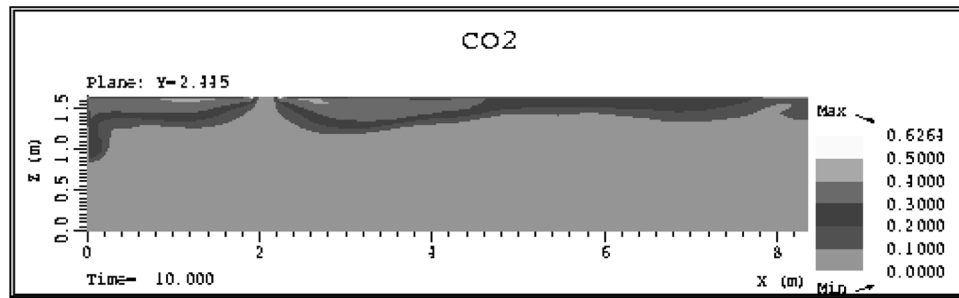


FIG. 11.  $\text{CO}_2$  contour plots along the cargo bay at the plane corresponding to the SPGG injector centerline at the end of injection (10s). Mean particle diameters are  $2\ \mu\text{m}$ .

gas temperature that is the cause of the heat flux. The greatest estimated heat flux is just under  $6836\ \text{W}/\text{m}^2$  with near-wall ceiling temperatures near  $1032\ \text{K}$ . Heat flux is linear in temperature so greater or lesser suppressant injection temperatures will lead to similar relative changes in heat flux. A nonlinear contribution to the heat flux arises from the buoyant forcing of the hot gases. Accounting for buoyancy, the heat flux is expected to change somewhat stronger than linearly with temperature. That means that a 10% reduction in injection temperature would lead to somewhat more than a 10% reduction in heat flux.

Fire suppression occurs through the joint effect of the particulate and the product gases ( $\text{CO}_2$ ,  $\text{H}_2\text{O}$ , and  $\text{N}_2$ ). These gases are transported throughout the cargo bay by the mean flow and the turbulent mixing. The distribution of  $\text{CO}_2$  along the injector plane at the end of injection is shown in Fig. 11 to represent the product gases. The association of the  $\text{CO}_2$  and other product gases with the high-temperature regions causes the highest concentrations of these gases to remain near the cargo bay ceiling.

The particle transport model described previously allows the prediction of the particle number density evolution in the cargo bay and also the evolution of the particle surface area. The particle surface area is indicative of the surface available for chemical reactions to occur that might play a role in suppressing flame chemistry. Figures 12 and 13 show the snapshots of surfaces of constant particle number density per volume for the  $2$  and  $15\ \mu\text{m}$  particles, respectively. Because the mass flux of particles is fixed by the propellant burn rate, the particle number density is inversely proportional to the particle mass. This results in higher density coverage for the smaller  $2\ \mu\text{m}$  particles shown in Fig. 12. The distribution of the number density at the end of the injection can also be viewed through the contour plot in Fig. 14. In addition to affecting the number density, the different momentum associated with differing particle sizes affect the wall-sticking behavior and the dispersion as will be described in the following paragraphs.

It can be observed in Figs. 12–14 that the particle number density on the left side of the domain (small values of  $x$ )

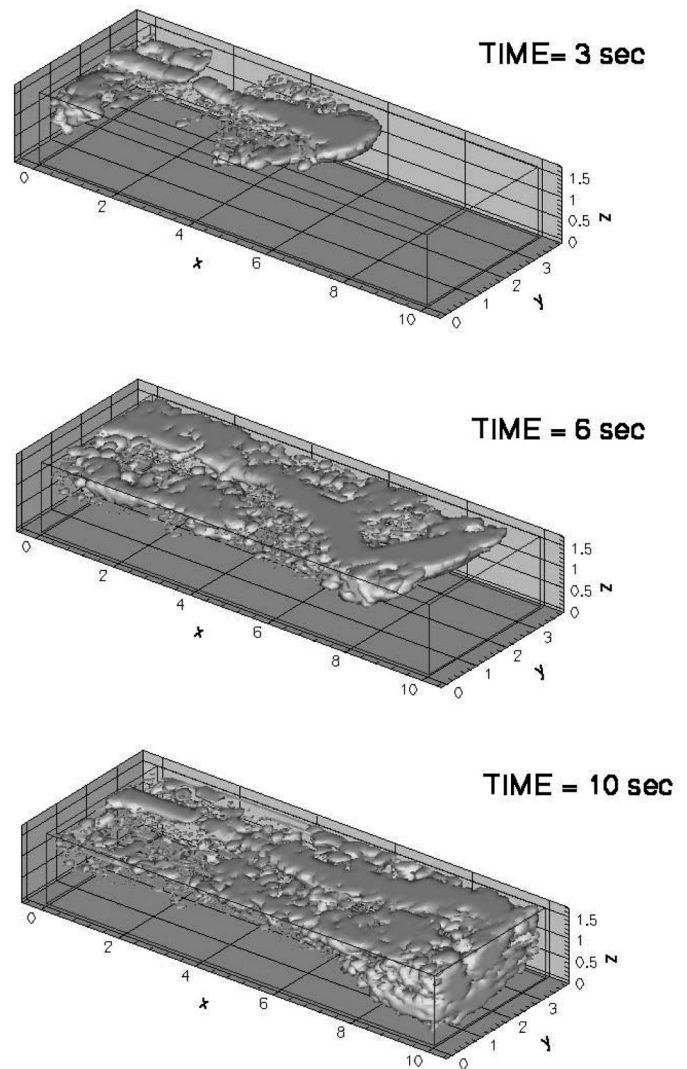


FIG. 12. Particle number density iso-surface plots at 3, 6, and 10s. The surface interior indicates the region where the particle number density exceeds  $10 \times 10^9\ \text{particles}/\text{m}^3$ . Mean particle diameters are  $2\ \mu\text{m}$ .

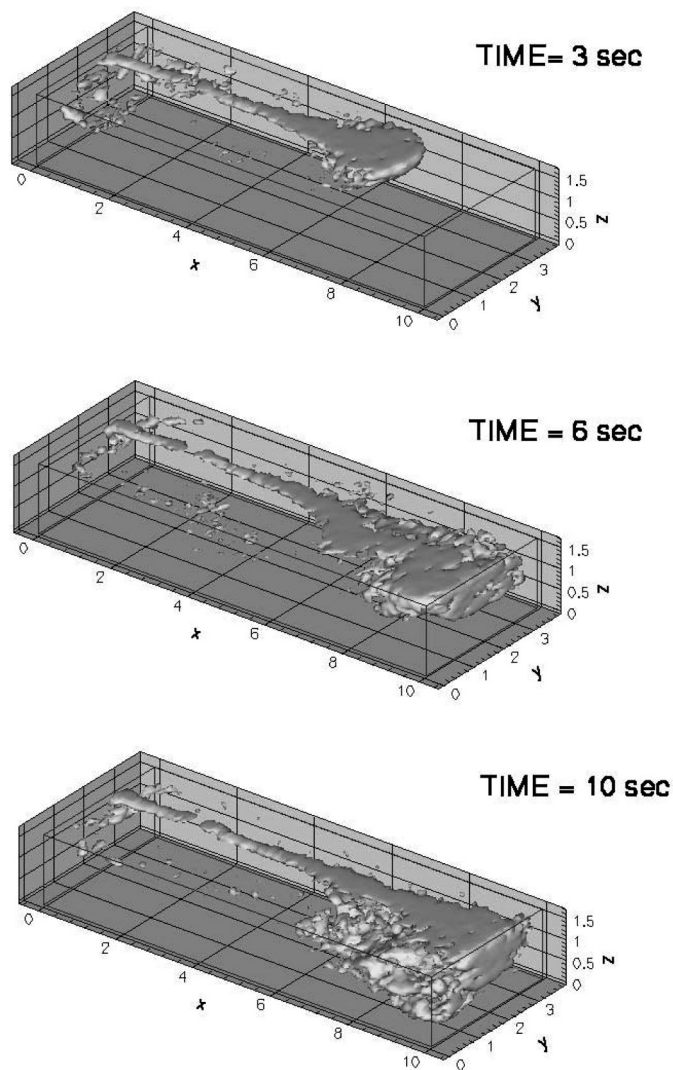


FIG. 13. As in Fig. 12 but with 15  $\mu\text{m}$  mean particle diameters.

is significantly less than on the right side. This asymmetry in the particle number density is attributable to the higher momentum of the flow along the ceiling and into the left wall. As the flow approaches the upper left corner, the gas is accelerated to follow the walls. The particles are also accelerated by the gas, but their velocities lag the gas velocity slightly. With higher mass, the particles accelerate to follow the gas more gradually and the velocity lag is greater. This higher momentum causes significantly more particles to “stick” to the left wall than the right wall. A greater fraction of the 15- $\mu\text{m}$  particles stick to the wall relative to the 2- $\mu\text{m}$  particles as a consequence of their greater momentum, as expected. Note that the particles, once they stick to the wall, are not transported further by the model.

It is also observed in Fig. 14 that the distribution of 15- $\mu\text{m}$  particles is more uniform over a particle number density range of  $1 \times 10^8$  to  $1 \times 10^{10}$  particles/ $\text{m}^3$  than the

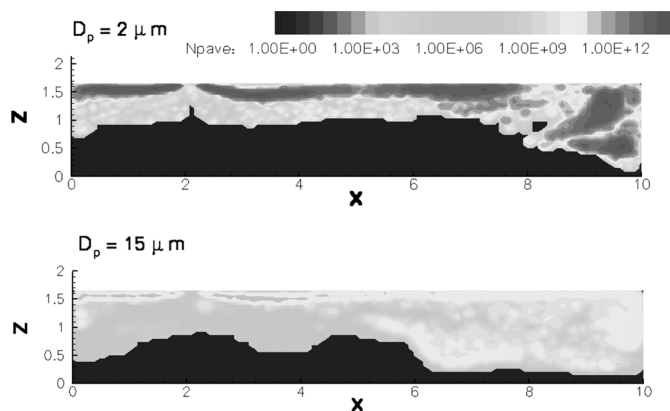


FIG. 14. Particle number density contour plots along the cargo bay at the plane corresponding to the SPGG injector centerline at the end of injection (10s). Mean particle diameters are 2  $\mu\text{m}$  (top) and 15  $\mu\text{m}$  (bottom).

distribution of 2- $\mu\text{m}$  particles. Conversely, there are regions of significantly higher number density, exceeding  $1 \times 10^{12}$  particles/ $\text{m}^3$  in the distribution of 2- $\mu\text{m}$  particles. The greater uniformity for larger particles arises from the effect of particle momentum in enhancing dispersion. In turbulent flows, particles experience intermittent acceleration in random directions due to turbulent fluctuations. Larger particles with greater momentum tend to travel farther as a consequence of this acceleration. For intermediate particle sizes like the 15- $\mu\text{m}$  particles studied herein, this leads to enhanced dispersion. Note that significantly larger particles have sufficient inertia that they are not affected by dispersion, so that dispersion is not monotonic in particle size. Rather, dispersion is maximized when the particle relaxation time, Eq. (4), is comparable to the turbulent mixing rate. With turbulent mixing times on the order of tenths of seconds relative to particle relaxation times of  $10^{-5}$  and  $10^{-3}$  s for 2 and 15  $\mu\text{m}$  particles are easily accelerated by turbulent fluctuations and the acceleration of larger particles to equivalent velocities carries them farther.

Figure 15 shows iso-surface plots for the surface area density, the particle surface area per unit volume, which is indicative of the available surface area for suppression reactions. Figure 16 shows the surface area density distribution along the injector centerline. The total surface area available for chemical activity per mass of injected agent increases as the particle size is reduced. If the particulate were evenly distributed, the available surface area would be on the order of  $1 \text{ m}^{-1}$  ( $1 \text{ m}^2$  of surface per cubic meter of volume) for the 15- $\mu\text{m}$  particles and  $8 \text{ m}^{-1}$  for the 2- $\mu\text{m}$  particles based on the injected mass and the chamber volume. Clearly, there is substantially more surface area available with smaller particles. However, the distribution of area is observed to be more uniform for the larger particles, as previously noted, due to enhanced turbulent dispersion.

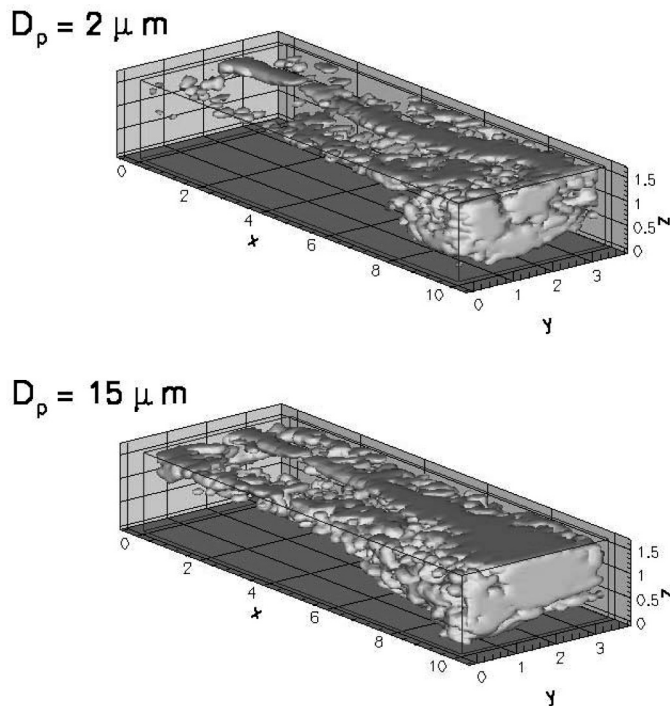


FIG. 15. Particle surface area density iso-surface plots at the end of injection (10 s). The surface interior indicates the region where the particle surface area density exceeds  $1 \text{ m}^{-1}$ . Mean particle diameters are  $2 \mu\text{m}$  (top) and  $15 \mu\text{m}$  (bottom).

This increased dispersion is responsible for the greater volume coverage for a surface density of  $1 \text{ m}^{-1}$  with larger ( $15 \mu\text{m}$ ) particles as shown in Figs. 15 and 16.

Previously in Figs. 12–14, the effect of particle size on the  $\text{KBr}/\text{K}_2\text{CO}_3$  particle distribution has been demonstrated. There are additional factors that might affect the

particle dispersion. Dispersion of these particles is roughly proportional to the turbulent fluctuations that are roughly proportional to the maximum flow velocities. Thus, another possible way to influence the distribution would be to change the mass burning rate or the injection slot area to change the velocity associated with injection; increased mass burning rate and reduced injection area should increase the dispersion rates. However, these changes are also likely to increase the number of particles impacting the wall and the net effect is unclear. Other questions arise as to particle deposition in the injector as a consequence of such changes. It is also possible to increase the particle dispersion by increasing the distance between the suppressant flow and the ceiling. Currently, the dispersion is only effective in one direction, downward, while the suppressant flows along the ceiling. Changing the injection angle or location to allow dispersion from the mean flow in all directions would increase the rate of dispersion. However, such changes need to account for the location of obstructions, namely the cargo that the system is designed to protect. The buoyant forcing of the suppressant plume is also a significant factor in reducing dispersion in the present flow. Buoyancy reduces downward dispersion because the hot gases, containing the particles, tend to rise toward the ceiling until the flow reaches the cargo bay side and end walls. Reductions in the suppressant temperature are likely to improve the mixing characteristics.

## CONCLUSIONS

A series of simulations have been conducted to study the dynamics of gas and particle flow through a simulated cargo bay during fire suppression with the Goodrich-244 suppression system. Detailed simulations of the propellant injector and the complete cargo bay show that the hot

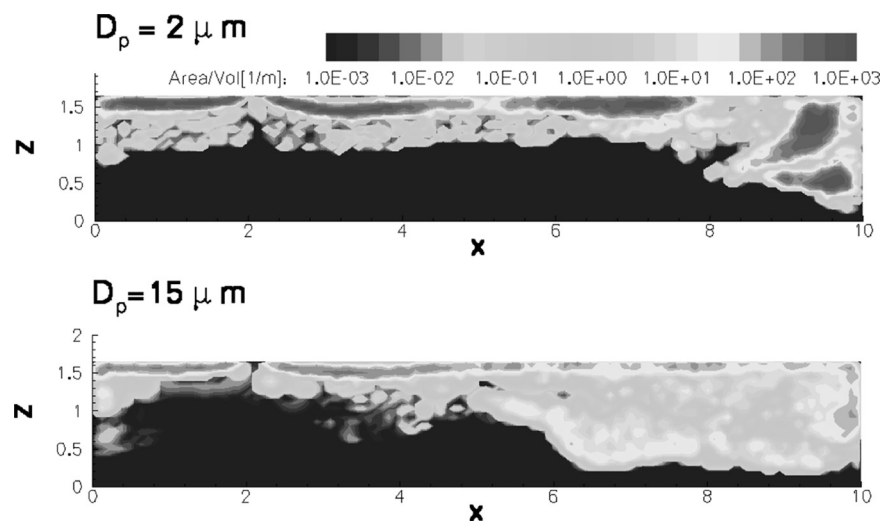


FIG. 16. Particle surface area density contour plots along the cargo bay at the plane corresponding to the SPGG injector centerline at the end of injection (10 s). Mean particle diameters are  $2 \mu\text{m}$  (top) and  $15 \mu\text{m}$  (bottom).

suppressant gases largely flow along the ceiling until the flow reaches the end walls, at which point the suppressant gases further mix through the cargo bay. This flow pattern results in relatively hot gas temperatures near the ceiling and heat fluxes as high as  $7 \text{ kW/m}^2$ . Particles comprising KBr and  $\text{K}_2\text{CO}_3$  are also present in the Goodrich-244 suppressant gases, and the simulations track the dynamics of these particles. Simulations were conducted using particles of both 2 and  $15 \mu\text{m}$ . Results for gas flow and particle dispersion with both models and both particle sizes are similar. Slower cooling of larger particles is observed to result in a greater delay in the cooling of the flow and an associated greater buoyant forcing. The particle size significantly affects the particle number density and the particle surface area available for chemical activity; smaller particles increase both of these quantities when measured globally (total particles or surface area per cargo bay volume). While larger ( $15 \mu\text{m}$ ) particles have significantly smaller overall number and area density than the smaller ( $2 \mu\text{m}$ ) particles, the larger particles are more evenly distributed.

#### ACKNOWLEDGEMENTS

The authors are grateful for the financial support provided by the Goodrich Corporation for this research. Sandia is a multiprogram laboratory operated by Sandia Corporation, a Lockheed Martin Company for the United States Department of Energy's National Nuclear Security Administration under contract DE-AC04-94AL85000. The first author acknowledges the partial support of this research provided by the Carbon Dioxide Reduction & Sequestration (CDRS) R&D Center of Korea.

#### REFERENCES

- Gann, R.G. *FY2004 Annual Report—Next Generation Fire Suppression Technology Program*, NIST Technical Note 1466; National Institute of Standards and Technology: Gaithersburg, MD, 2005.
- Hamins, A.; Gmurczyk, G.W.; Grosshandler, W.L.; Rehwoldt, R.G.; Vazquez, I.; Cleary, T.; Presser, C.; Seshadri, K. Flame suppression effectiveness. In *Evaluation of Alternative In-Flight Fire Suppressants for Full-Scale Testing in Simulated Aircraft Engine Nacelles and Dry Bays Section 4*; Grosshandler, W.L., Gann, R.G., Pitts, W.M., Eds.; Washington, DC, 1994; 345–465.
- Olander, D.E. Development and testing of Goodrich 244 fire suppressant. *Proceedings of the 12th Halon Options Technical Working Conference*; Albuquerque, NM, April 30–May 2, 2002.
- Noto, T.; Babushok, V.I.; Hamins, A.; Tsang, W. Inhibition effectiveness of halogenated compounds. *Combustion and Flame* **1998**, *112* (1&2), 147–160.
- Gritzo, L.A.; Sivathanu, Y.R.; Gill, W. Transient measurements of radiative properties, soot volume fraction and soot temperature in a large pool fires. *Combustion Science and Technology* **1998**, *139*, 113–136.
- Jones, W.P.; Launder, B.E. Prediction of laminarization with a 2-equation model of turbulence. *International Journal of Heat and Mass Transfer* **1972**, *20*, 301–314.
- Holen, J.; Brostrom, M.; Magnussen, B.F. Finite difference calculation of pool fires. *Proceedings of the Combustion Institute* **1990**, *23*, 1677–1683.
- Patankar, S.V. *Numerical Heat Transfer and Fluid Flow*; Taylor & Francis: London, 1980.
- Faeth, G.M. Mixing, transport and combustion in sprays. *Progress in Energy and Combustion Science* **1987**, *13*, 293–345.
- Gosman, A.D.; Ioannides, E. *Aspects of Computer Simulation of Liquid-Fueled Combustors*, AIAA Paper 81-0323; St. Louis, MO, 1981.
- Shuen, J.S.; Chen, L.D.; Faeth, G.M. Evaluation of a stochastic model of particle dispersion in a turbulent round jet. *AIChE Journal* **1983**, *29* (1), 167–170.
- Zhou, Q.; Yao, S.C. Group modeling of impacting spray dynamics. *International Journal of Heat and Mass Transfer* **1992**, *35* (1), 121–129.
- Dukowicz, J.K. A particle fluid numerical model for liquid sprays. *Journal of Computational Physics* **1980**, *35* (2), 229–253.
- Amsden, J.; Ramshaw, D.; O'Rourke, P.; Dukowicz, J.K. *KIVA: A Computer Program for Two- and Three-Dimensional Fluid Flows with Chemical Reactions and Fuel Sprays*, Los Alamos Report LA-10245; Los Alamos, NM, 1985.
- Reitz, R.D. Modeling atomization processes in high-pressure vaporizing sprays. *Atomization and Spray Technology* **1987**, *3*, 309–337.
- Sirignano, W.A. *Fluid Dynamics and Transport of Droplets and Sprays*; Cambridge University Press: New York, 1999.
- Chhabra, R.P.; Agarwal, L.; Sinha, N.K. Drag on non-spherical particles: An evaluation of available methods. *Powder Technology* **1999**, *101*, 288–295.
- Ganser, G.H. A rational approach to drag prediction of spherical and nonspherical particles. *Powder Technology* **1993**, *77*, 143–152.
- Radhakrishnan, K.; Hindmarsh, A.C. *Description and Use of LSODE, the Livermore Solver for Ordinary Differential Equations*, Technical Report UCRL-ID-113855; Lawrence Livermore National Laboratory: Livermore, CA, 1993.
- DesJardin, P.E.; Gritzo, L.A. *A Dilute Spray Model for Fire Simulations: Formation, Usage and Benchmark Problems*, Technical Report SAND2002-3419; Sandia National Laboratory: Albuquerque, NM, 2002.